Modelling enhanced confinement in drift-wave turbulence

R. J. Hajjar, P. H. Diamond, A. Ashourvan, and G. R. Tynan

Citation: Physics of Plasmas **24**, 062106 (2017); doi: 10.1063/1.4985323
View online: http://dx.doi.org/10.1063/1.4985323
View Table of Contents: http://aip.scitation.org/toc/php/24/6
Published by the American Institute of Physics

Modelling enhanced confinement in drift-wave turbulence

R. J. Hajjar, P. H. Diamond, A. Ashourvan, and G. R. Tynan
Mechanical and Aerospace Engineering Department, University of California, San Diego, 9500 Gilman Drive - La Jolla, California 92093, USA

(Received 3 January 2017; accepted 22 May 2017; published online 12 June 2017)

The results of modeling studies of an enhanced confinement in the drift wave turbulent plasma of the CSDX linear device are presented. The mechanism of enhanced confinement is investigated here using a reduced 1D, time-dependent model, which illustrates the exchange of enstrophy between two disparate scale structures: the mesoscale flow and profile, and the turbulence intensity fields. Mean density, mean vorticity, and turbulent potential enstrophy are the variables for this model. Total potential enstrophy is conserved in this model. Vorticity mixing occurs on a scale length related to an effective Rhines' scale of turbulence, and shrinks as both density and vorticity gradients steepen. Numerical results obtained from solution of the model agree well with the experimental data from CSDX showing: (i) a steepening of the mean density profile, indicating a radial transport barrier formation, (ii) the development of a radially sheared azimuthal flow velocity that coincides with the density steepening and initiates a turbulence quench, and (iii) negative Reynolds work values, indicating that fluctuations drive the shear flow. These observations as the magnitude of the magnetic field B increases are recovered using *purely diffusive* expressions for the vorticity and density fluxes. A new dimensionless turbulence parameter R_{DT}-defined as the ratio of the integrated potential enstrophy transfer from turbulence to the flow, to the integrated potential enstrophy production due to relaxation of the density gradient is introduced as a turbulence collapse indicator that detects when the enhanced confinement state is triggered. *Published by AIP Publishing.*
[http://dx.doi.org/10.1063/1.4985323]

I. INTRODUCTION

Turbulent phenomena and their evolving properties in fluids are topics of both classical and current significance. Of particular interest are the spectral features and transport properties of turbulence in magnetized plasmas. Density and temperature gradients, typically present near the edges of large scale magnetically confined devices, generate fluctuations that give rise to fully developed drift wave (DW) instabilities. Such instabilities carry fluxes via cross-field transport and limit the energy confinement time τ_E.[1,2] Suppression of these instabilities and reduction of the cross-field transport rates are therefore essential requirements for achieving enhanced confinement, in ITER and future tokamaks.

One way the plasma itself mitigates cross-field transport rates is via fluctuation driven zonal flows (ZFs). In laboratory plasmas, zonal flows are strongly sheared $\mathbf{E}\times\mathbf{B}$ layers. Generated via Reynolds stresses and particle transport, zonal flows arise when low-frequency drift modes interact by modulational instability or via an inverse cascade, to form a large scale anisotropic structure. The direct relation between microscale drift waves and macroscale zonal flows has been already well established both theoretically[3] and experimentally,[4,5] so much so that the system is now referred to as" drift wave-zonal flow turbulence" (see Ref. 6 for a detailed review).

Interaction between separate components of the DW-ZF turbulence is found to affect the turbulent transport dynamics. Experimental studies in both linear and toroidal devices show that the state of turbulence changes with the magnetic field (CSDX),[7,8] the filling gas pressure (LMDU),[9] and the radial electric field (KIWI).[10] Shearing of the DW structures leads to an energy transfer between low frequency fluctuations and vortices with finite azimuthal mode numbers, including $m\sim 0$ zonal flows. This coupling initiates a process of depletion of the fluctuation energy, which may continue to the point of the collapse of the turbulence intensity. When sufficient heat source, torque, and fueling are available, a thermally insulation layer supported by a strongly sheared $\mathbf{E}\times\mathbf{B}$ flow is formed. A transport barrier is thus created and an enhanced confinement regime occurs.[11–13] The concept of shear enhanced turbulence decorrelation was proposed nearly three decades ago.[14,15] Since then, several variations on the theme of the predator-prey model describing the interplay between turbulent fluctuations and $\mathbf{E}\times\mathbf{B}$ sheared flows have been suggested to explain the plasma evolution towards an enhanced confinement state in fusion devices like TJ-II,[16] NSTX,[17] and EAST.[18] Moreover, net inward fluxes would often accompany this transition, as it was observed in various toroidal[19,20] and small scale linear devices.[21–23]

In CSDX, early observations showed a controlled transition from nonlinearly coupled eigenmodes to fully developed broadband turbulence in the plasma, as the magnitude of B is increased.[24] Recent studies revealed the existence of an enhanced regime at $B=1200\,G$, associated with a steepening of the mean density profile, the development of a strong velocity shearing and turbulent kinetic energy coupling to the flow. An inward particle flux as well as a change in the global and local turbulence features were also observed.[25,26]

We present a reduced 1D transport model that describes the space-time evolution of turbulence and mean fields in the

turbulent plasma conditions of CSDX. The model is formulated in terms of potential vorticity dynamics, and conserves total potential enstrophy.[27] All evolution is expressed in terms of the particle and vorticity fluxes. Flux nonlinearity enters via a gradient dependent mixing length, and the vorticity flux includes both a diffusive and a residual component. The model recovers profile evolution in CSDX with increasing B, without the need to include an explicit inward particle pinch in the expression for the particle flux. This evolution corresponds to: (i) steepening of the mean density profile as a signature of a enhanced confinement (ii) the development of a radially sheared azimuthal flow velocity that triggers the transition to an improved energy confinement state, and (iii) negative Reynolds work values indicating that energy is transfered to flow as the system self-organizes. We mention here that the Reynolds work sign convention used in Refs. 25 and 26 is opposite to the one adopted here; a positive Reynolds work in Refs. 25 and 26 indicates a turbulence decay and a zonal flow drive. The model can also be used to study the effects of other factors on the dynamics of this global transition. These factors include: presence of a thin layer of neutrals around the plasma, variations of the plasma ion fueling intensity S and of the macroscopic turbulent mixing length l_0 to be defined in Sec. III. The model is used to investigate the relevant case of a plasma with a high collisional Prandtl number: $Pr = \nu_c/D_c$.

The remainder of this paper is organized as follows: Sec. II presents the model, with a discussion of the corresponding physics and assumptions. This requires an explanation of the expression for the mixing length l_{mix}, and a review of the physics behind the Rhines' scale. Expressions for the density, vorticity, and potential enstrophy fluxes and coefficients are also presented in this section, along with the three spatio-temporal equations of the model. Section III reports on the numerical results obtained when varying the magnitude of the magnetic field. A diffusive vorticity flux: $\Pi = -\chi\nabla u$, where the vorticity $u = \nabla^2\Phi$, is first used in Section III. A residual stress Π_{res} is then included in the vorticity flux expression: $\Pi = \Pi_{res} - \chi\nabla u$ to assess its potential role. A set of local and global validation metrics are then presented in Section IV in order to verify that the model truly describes the plasma evolution as it occurs in CSDX. Section V explores the energy exchange between fluctuations and the mean flow and studies time variations of two parameters; R_T already introduced in a previous work[28] and a new parameter R_{DT}, derived from this model. Both parameters provide quantitative and qualitative measurements of this exchange, and serve as turbulence collapse indicators. Conclusions are drawn in Sec. VI.

II. STRUCTURE OF THE 3-FIELD REDUCED MODEL

The proposed model investigates space and time variations of the following three fields: the mean density $\langle n\rangle$, the mean vorticity $\langle u\rangle = \langle\nabla^2\Phi\rangle$, and the turbulent potential enstrophy $\varepsilon = \langle\frac{(\tilde{n}-\tilde{u})^2}{2}\rangle$. It is derived from the collisional Hasegawa-Wakatani equations[29,30]

$$(\partial_t - \nabla\Phi\times\hat{z}.\nabla)\nabla^2\Phi = -c_1\nabla_\parallel^2(\Phi - n) + c_2\nabla^4\Phi, \quad (1a)$$

$$(\partial_t - \nabla\Phi\times\hat{z}.\nabla)(n + \ln n_0) = -c_1\nabla_\parallel^2(\Phi - n). \quad (1b)$$

Here, $c_1 = T_e/e^2n_0\eta\omega_{ci}$ and $c_2 = \mu/\rho_s^2\omega_{ci}$. μ and η are the ion viscosity and plasma resistivity, n_0 is the average plasma density, and n and Φ are the normalized fluctuating density and potential. CSDX plasma being collisional, a modified Hasegawa-Wakatani model can be used to describe turbulent transport in this device. In addition, LIF measurements in CSDX show that the axial flow is well within the subsonic limit.[31] Thus, the radial gradient of the parallel velocity reported as contributing to an inward particle flux in Ref. 32 does not contribute to such a flux here, as a parallel shear flow instability simply cannot be triggered.[33] This fact is taken into account while formulating the model. Our reduced model relies on two related points: conservation of the total potential enstrophy PE (mean and turbulent) up to dissipation and external forcing, and inhomogeneous potential vorticity (PV) mixing via vorticity diffusion. This mixing occurs on a scale l_{mix} that is an interpolation between an excitation scale l_0 and the Rhines' scale of turbulence l_{Rh}. Dynamic dependence of l_{mix} on l_{Rh} results from the interaction between the mean fields and the turbulence structures, and allows the model to capture the internal energy exchange during this interaction. The Rhines' scale is inversely proportional to the potential vorticity gradient $\nabla q = \nabla n - \nabla u$; hence, l_{mix} has also an inverse dependence on ∇q and shrinks as ∇u and ∇n steepen. The model uses purely diffusive expressions for the turbulent field fluxes *without* an explicit pinch velocity contribution to the particle flux. In fact, local expressions for the fluxes of n, u, and ε as derived using the quasi-linear theory are:[34] $\Gamma_n = -D_n\nabla n$, $\Gamma_\varepsilon = -D_\varepsilon\nabla\varepsilon$, and $\Pi = \Pi_{res} - \chi\nabla u$. A discussion of the diffusion coefficients and the residual vorticity stress is referred to Subsecs. II A and II B.

A full derivation of the model is available in Ref. 27. We mention here only the relevant equations

$$\partial_t u = -\partial_x\Pi + \mu_c\nabla^2 u, \quad (2a)$$

$$\partial_t n = -\partial_x\Gamma_n + D_c\nabla^2 n, \quad (2b)$$

$$\partial_t\varepsilon = -\partial_x\Gamma_\varepsilon + P - \varepsilon^{3/2} - (\Gamma_n - \Pi)(\partial_x n - \partial_x u), \quad (2c)$$

for mean density n and mean vorticity fields u, as well as for fluctuating potential enstrophy $\varepsilon = (\tilde{n}/n_0 - \rho_s^2\nabla^2 e\tilde{\Phi}/T_e)^2/2$. Here, the fields are expanded into a mean and a fluctuating part: $n = \langle n\rangle + \delta n$, $\mathbf{v}_E = \langle v\rangle\hat{y} + \delta\mathbf{v}$, $u = \langle u\rangle + \delta u = \partial_x\langle v\rangle + \delta u$. Fluxes of turbulent vorticity, density, and potential enstrophy fluxes are: $\Pi = \langle\delta v_x\delta u\rangle$, $\Gamma_n = \langle\delta v_x\delta n\rangle$ and $\Gamma_\varepsilon = \langle\delta v_x\delta q^2\rangle$, respectively. Turbulent enstrophy is related to the fluctuating potential vorticity $\delta q = \delta n - \delta u$ via: $\varepsilon = \langle\delta q^2\rangle/2$. μ_c and D_c are plasma collisional viscosity and diffusivity, n and Φ are normalized to n_0 and T_e/e, space and times scales are normalized to $\rho_s = \sqrt{m_iT_e}/eB$ and $1/\omega_{ci} = m_ic/eB$.

The first terms of the RHS of Eqs. (2a)–(2c) represent a turbulent diffusive flux or spreading of the corresponding field. In Eq. (2c), P represents the enstrophy production due to an external stirring, and replaces explicit linear instability

which is not treated in this model. Note that in this model formulation, the forcing serves only to initialize a background turbulence level. It does not represent the turbulence drive in the steady state. Drive is due to ∇n relaxation, i.e., $\Gamma_n \nabla n$ term in Eq. (2c). The turbulence and transport results are insensitive to the initializing forcing, and we write it as: $P = \sqrt{\varepsilon}(u_0^2 - \varepsilon)$. This form of P reflects generation of enstrophy via external stirring. Other forms of $P \propto \varepsilon$ are equally valid and generate similar results. Enstrophy dissipation, proportional to $\varepsilon^{3/2}$, is a direct outcome of the forward enstrophy cascade associated with nonlinear dissipation of ε at smaller scales. The last term of Eq. (2c) is a direct coupling between the vorticity and density fluctuations, and is interpreted as an internal production of potential enstrophy. As PV mixing occurs, mean PE values are converted into turbulent ones and vice versa, while total PE is conserved. Equations (2a)–(2c) constitute a closed system that can be solved numerically once expressions for the field fluxes are known. Since the model is diffusive, expressions for the diffusion coefficients and the corresponding mixing length are thus needed.

Although CSDX is a cylindrical plasma, the previous equations are written in a 1D form. This results from taking the axial and azimuthal average of the density, vorticity, and enstrophy fields in order to obtain the corresponding mean quantities: $\langle n(r)\rangle$, $\langle u(r)\rangle = \langle \nabla^2 \Phi\rangle$ and $\langle \varepsilon(r)\rangle$.

A. The mixing length

Central to the formulation of a Fickian flux is the use of a mixing length l_{mix}. In this model, l_{mix} is an interpolation between the external excitation dimension l_0 and the Rhines' scale of turbulence l_{Rh}.[35] The dimension l_0 is known from experiment, and thus, an investigation of l_{mix} requires a study of the physics behind the Rhines' scale. In 3D turbulence, vortex stretching leads to enstrophy production that drives the fluid energy to smaller scales until it is removed from the system by viscous dissipation. However, in quasi 2D turbulence, vortex stretching is by definition inhibited and other nonlinear processes, such as vortex merging, play the prominent role. In the 2D case, energy undergoes an *inverse energy cascade* towards larger scales, which explains the emergence of large scale jets from small scale turbulent structures. As eddies become bigger, their size increases and their overturning slows, which makes their dynamics much more wave-like. The Rhines' scale l_{Rh} can be interpreted as a transition length scale between a turbulence dominated regime and wave-like dynamics,[35] and is obtained by balancing the turbulence characteristic rate, i.e., the eddy turnover rate, with the wave frequency. In a DW system, an estimate of the eddy turnover rate is: $1/\tau_c \approx \delta v/l_{Rh} \approx \sqrt{\varepsilon}$, while the drift wave frequency is: $\omega \approx -k_y v_{De}/(1 + k_\perp^2 \rho_s^2) \approx l_{Rh}\nabla q$, where v_{De} is the electron diamagnetic drift velocity. Balancing these two scales then gives: $l_{Rh} \approx \sqrt{\varepsilon}/\nabla q = \sqrt{\varepsilon}/\nabla(n-u)$.

In our model, l_0 and l_{Rh} are the two significant length scales of the system. When $l_0 \ll l_{Rh}$, the vorticity gradient is weak, and the natural estimate of the mixing length is simply the external dimension: $l_{mix} \sim l_0$. This prescription however is not accurate in the case of a strong vorticity gradient, where ∇q can no longer be neglected. In this case, when the Rhines' scale is much smaller than the stirring dimension ($l_{Rh} \ll l_0$), coupling between different scales is stimulated. A reasonable estimate of the mixing length is then obtained by balancing the mean kinetic energy dissipation rate and the mean PV gradient frequency.[36] The Rhines' scale is then the governing spatial structure for turbulence mixing in these cases of steep PV gradients, generating $l_{mix} \sim l_{Rh}$. In between these two limiting cases, one should include the effect of finite drift-Rossby frequency in l_{mix}. This is achieved by writing l_{mix} as an interpolation between l_0 and l_{Rh},

$$l_{mix}^2 = \frac{l_0^2}{1 + (l_0/l_{Rh})^2} = \frac{l_0^2}{1 + l_0^2(\partial_x(n-u))^2/\varepsilon}. \tag{3}$$

B. Expressions for the turbulent fluxes

Expressions for the turbulent density and vorticity fluxes were previously derived using quasi-linear theory.[34] In the near adiabatic regime in which parallel diffusion timescale is the smallest characteristic time scale of the system, and in the absence of any shear, the drift wave frequency is $\omega^\star = \omega_{\mathbf{m}}^r = v_d k_m/(1 + k_\perp^2)$ where $k_\perp^2 = -\nabla_\perp^2 \Phi/\Phi$. Expressions for the fluxes and the diffusion coefficients are

$$\Gamma_n = -D_n \partial_x \langle n\rangle, \tag{4a}$$

$$\Pi = (\chi - D_n)\partial_x\langle n\rangle - \chi\partial_x^2\langle v\rangle = \Pi_{res} - \chi\partial_x\langle u\rangle, \tag{4b}$$

$$D_n = \sum_{\mathbf{m}} \frac{k_\perp^2}{1 + k_\perp^2}\frac{k_m^2}{\alpha_n}\langle \delta\phi_{\mathbf{m}}^2\rangle, \tag{4c}$$

$$\chi = \sum_{\mathbf{m}} \frac{|\gamma_m|}{|V_0 - \omega_{\mathbf{m}}/k_m|^2}\langle \delta\phi_{\mathbf{m}}^2\rangle. \tag{4d}$$

Here, the dimensionless electron drift velocity is $v_d(x) = -d\ln n_0(x)/dx = \chi\nabla n$ and the plasma flow velocity is $V_0 = \langle v\rangle$. The mode number is $\mathbf{m} = (m,n,l)$ with m, n, and l being the azimuthal, axial, and radial mode numbers, respectively. $\omega_{\mathbf{m}} = \omega_{\mathbf{m}}^r + i|\gamma_{\mathbf{m}}|$ is the mode eigenfrequency, k_m and $k_\parallel$ are the azimuthal and parallel wave numbers, and $\alpha_n = \eta k_\parallel^2$ is the parallel diffusion rate.

The residual stress Π_{res} in Eq. (4b) originates from a decomposition of the Reynolds stress into diffusive and non-diffusive components, and appears when the off-diagonal terms of the poloidal Reynolds stress do not vanish. This results as a consequence of a symmetry breaking mechanism in $\langle k_r k_\theta\rangle$ where $\langle\ldots\rangle$ is a spectral average.[37,38] Physically, Π_{res} converts parts of the diving particle flux to an azimuthal flow. Π_{res} is responsible for generation of plasma flows through the density gradient, even in the absence of any magnetic shear.[39] Using quasi-linear theory, the residual stress $\Pi_{res} = \Gamma_n/n - \chi v_d$.[34] In the adiabatic regime, the first term in the expression of Π_{res} is negligible with respect to the second one, simply because it is proportional to $1/\alpha_n$ and $\alpha_n \gg 1$. One can thus label it as the non-adiabatic term. When no flow is present, or when the flow velocity V_0 is constant, the vorticity flux reduces to Π_{res}. Writing $\Gamma_\varepsilon = -D_\varepsilon \partial_x \varepsilon$ and plugging in

the model equations, we obtain the final form for the three field equations,

$$\partial_t n = \partial_x[D_n \partial_x n] + D_c \partial_x^2 n, \tag{5a}$$

$$\partial_t u = \partial_x[\chi \partial_x u] + \mu_c \partial_x^2 u - \partial_x[\Pi_{res}], \tag{5b}$$

$$\partial_t \varepsilon = \partial_x[D_\varepsilon \partial_x \varepsilon] + \Pi_{res}(\partial_x n - \partial_x u) - (\chi \partial_x u - D_n \partial_x n) \times (\partial_x n - \partial_x u) - \varepsilon^{3/2} + \sqrt{\varepsilon}(u_0^2 - \varepsilon). \tag{5c}$$

Equations (5a)–(5c) are rearranged and integrated to give

$$\int_0^L \partial_t \left(\varepsilon + \frac{(n-u)^2}{2}\right) dx = \int_0^L \big(P - \varepsilon^{3/2} - \partial_x \Gamma_\varepsilon - (\Gamma_n - \Pi)(\partial_x n - \partial_x u) + (n-u)(\partial_t n - \partial_t u)\big) dx = \int_0^L (P - \varepsilon^{3/2}) dx \tag{6}$$

after neglecting the terms proportional to D_c and μ_c. This shows that the system conserves total PE up to forcing and dissipation, as a result of enstrophy exchange between mean fields and fluctuations. The internal turbulent PE production term is canceled by the corresponding loss term in the evolution equation for the mean PE as a part of this enstrophy exchange. In view of the total PE conservation elucidated above, we go back to Eq. (3) to emphasize how crucial the expression for l_{mix} is in closing the feedback loop between the PV gradient and the corresponding diffusion coefficient: as $\nabla q = \nabla n - \nabla u$ steepens, the mean potential enstrophy $\frac{(n-u)^2}{2}$ increases, causing a drop in turbulent potential enstrophy ε as a result of total PE conservation. When ε decreases, the mixing length and thus the corresponding PV diffusion coefficient shrink, leading to a further increase in the PV gradient. Hence, a closed feedback loop is generated.

C. Viscosity and diffusion coefficients

In the near adiabatic regime, the timescale ordering is: $\eta \kappa_\parallel^2 \gg \omega \gg V_0'$. Using $|k_m^2 \langle \delta\phi_{\mathbf{m}}^2 \rangle| = |\langle \delta v_{\mathbf{m}}^2 \rangle| \approx l_{mix}^2 \varepsilon$, the particle diffusion coefficient D_n is

$$D_n = \varepsilon l_{mix}^2 / \alpha, \tag{7}$$

where the resistive parallel diffusion rate $\alpha = (1 + k_\perp^2)\alpha_n / k_\perp^2$. From dimensional analysis, α is proportional to $\sqrt{\varepsilon}$ and the particle diffusion coefficient is: $D_n = l_{mix}^2 \sqrt{\varepsilon}$.

As for the vorticity diffusion coefficient, χ is not dominated by a large resistive parallel diffusion rate. Unlike the expression for D_n, the denominator of Eq. (4d) represents the competition between the flow shear V_0' and the wave frequency ω. In the absence of shear, instabilities are density gradient driven collisional DWs that are damped by viscous dissipation. Their growth rate is then that of a drift wave: $|\gamma_{DW}| = (\omega_m^2/\alpha_n)(k_\perp^2/(1+k_\perp^2)) = \omega_m^2/\alpha$, reduced by the dissipation rate $|\gamma_\mu|$. The vorticity diffusion coefficient is then

$$\chi = \sum_{\mathbf{m}} \frac{(|\gamma_{DW}| - |\gamma_\mu|)|k_m^2 \langle \delta\phi_{\mathbf{m}}^2 \rangle|}{\omega_m^2} = \sum_m \frac{\frac{\omega_m^2}{\alpha} |k_m^2 \langle \delta\phi_{\mathbf{m}}^2 \rangle|}{\omega_m^2} \sim \frac{\varepsilon l_{mix}^2}{\alpha}.$$

When a flow shear V_0' is present, the vorticity diffusion coefficient χ is reduced, as the net turbulence correlation time decreases. When incorporating the shear effect into the turbulence correlation time, $1/\alpha$ becomes: $1/\alpha \simeq 1/\sqrt{(k_\perp \delta v)^2 + (V_0')^2} \simeq 1/\sqrt{\varepsilon + q^2}$, reflecting enstrophy generation and presence of flow shear, respectively. The vorticity diffusion coefficient χ then becomes

$$\chi = \varepsilon l_{mix}^2 / \sqrt{\varepsilon + q^2} = l_{mix}^2 \varepsilon / \sqrt{\alpha^2 + c_u u^2}. \tag{8}$$

Here, a coefficient c_u reflecting the strength of the shear flow has been added to the expression of χ. We will show later on that the numerical solutions for this model are insensitive to the parameter c_u. In a stationary regime, $\sqrt{\varepsilon} > q$ and the vorticity coefficient $\chi = \sqrt{\varepsilon} l_{mix}^2$ found previously[40] is recovered. In a strong shear regime where $q > \sqrt{\varepsilon}$, the vorticity coefficient is $\chi = \varepsilon l_{mix}^2 / |q|$. Finally, we use the following expression for D_ε: $D_\varepsilon = l_{mix}^2 \varepsilon / \alpha$. We mention here that the model includes three different time scales: the wave frequency and growth rate inverse time scales ω_m^{-1} and $|\gamma|^{-1}$ appearing in the spectral sums of the diffusion coefficients expressions, the correlation or eddy turnover time $\varepsilon^{-1/2}$ appearing in the enstrophy equation, and a diffusive time scale which characterizes the evolution of the mean field quantities as a result of turbulent fluxes evolution. While the first two are fast time scales, the last one is a slow (diffusive) one.

III. MODEL PREDICTIONS OF PLASMA PROFILES

In order to compare the model predictions to the experimental results obtained from CSDX, we present in this section the density and vorticity profiles numerically predicted by the model for different B values. Two forms of vorticity fluxes are considered. First, a diffusive vorticity form: $\Pi = -\partial_x u$. Then, a residual stress Π_{res} is added to the vorticity flux. The two cases are then compared to evaluate any potential role of Π_{res}. Before proceeding, we lay out the experimental parameters of CSDX cylindrical magnetized helicon plasma: the plasma column has a total length $L = 2.8$ m and a radius $a = 10$ cm. Argon plasma with the following characteristics is produced: $n_e = 10^{13}\text{cm}^{-3}$, $T_e = 4$eV, and $T_i = 0.3 - 0.7$ eV. The magnitude of the magnetic field B ranges between 800 and 1300 G, giving $\omega_{ci}^{-1} \approx 30\,\mu$s and $\rho_s = C_s/\omega_{ci} \approx 1$ cm where $C_s = \sqrt{T_e/m_i}$ is the plasma sound speed. Argon neutrals are radially injected at a constant flow rate of 25 sccm, and the corresponding neutral gas pressure $P_{gas} = 3.2$ mTorr is equivalent to a neutral density $n_n = 10^{14}\text{cm}^{-3}$.[25,26] Plasma neutral ionization rate at $T_e = 5$ eV is $S = n_e n_n \langle \sigma_{ion} v_e \rangle = 10^{17}\text{cm}^{-3}s^{-1}$, where $\langle \sigma_{ion} v_e \rangle = 10^{-10}\text{cm}^3/\text{s}$ is the ionization rate coefficient at 5 eV. These values will be used in our calculations, in order to benchmark our model predictions to the experimental results (see Fig. 1).

A. Diffusive vorticity flux: $\Pi = -\chi \partial_x u$

1. Model equations

For a shear strength parameter $c_u = 0$ and $\alpha = \sqrt{\varepsilon}$, the diffusion coefficients are equal: $D_n = \chi = D_\varepsilon = l_{mix}^2 \varepsilon^{1/2}$ and $\Pi_{res} = 0$. The vorticity flux is then: $\Pi = -\chi \partial_x u$.

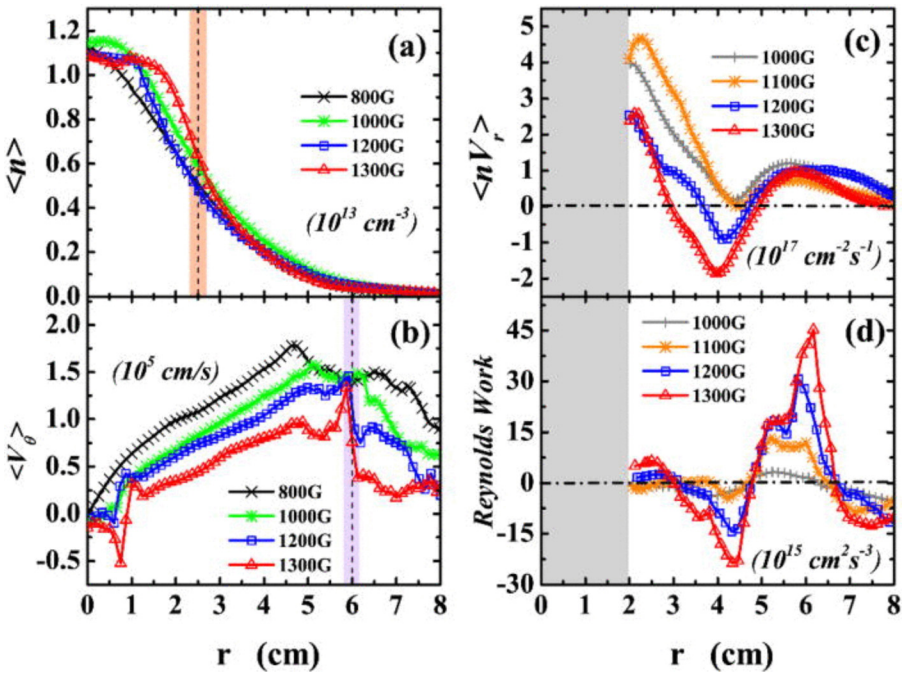

FIG. 1. Experimental plasma profiles at different magnetic field values. Reprinted with permission from Phys. Plasmas **22**, 050704 (2015). Copyright 2015 AIP Publishing LLC.[25]

Equations (5a)–(5c) are rescaled using: $x \equiv Lx$, $\varepsilon \equiv u_0^2\varepsilon$, $n \equiv Lu_0 n$, $u \equiv Lu_0 u$, $t \equiv L^2 t/u_0$, $\mu_c \equiv u_0\mu_c$ and $D_c \equiv u_0 D_c$,

$$\partial_t n = \partial_x\left[\frac{l_0^2\varepsilon^{3/2}\partial_x n}{\varepsilon + l_0^2(\partial_x(n-u))^2} + D_c\partial_x n\right] + S, \tag{9a}$$

$$\partial_t u = \partial_x\left[\frac{l_0^2\varepsilon^{3/2}\partial_x u}{\varepsilon + l_0^2(\partial_x(n-u))^2} + \mu_c\partial_x u\right], \tag{9b}$$

$$\partial_t\varepsilon = \partial_x\left[\frac{l_0^2\varepsilon^{3/2}\partial_x\varepsilon}{\varepsilon + l_0^2(\partial_x(n-u))^2}\partial\varepsilon\right] + L^2\left[\frac{l_0^2\varepsilon^{3/2}(\partial_x(n-u))^2}{\varepsilon + l_0^2(\partial_x(n-u))^2} - 2\varepsilon^{3/2} + \sqrt{\varepsilon}\right]. \tag{9c}$$

Here, L is the total plasma column length and S (normalized to $n_0 = 10^{13}\,\mathrm{cm}^{-3}$) is the external fueling source for ion density. The latter represents the combination of continuous neutral injection and the ionization energy provided by the external source of heat, i.e., CSDX external antenna. Parameters of Eqs. (9a)–(9c) are rescaled to their dimensional form to express the B dependence: $t \equiv t/\omega_{ci}$ and $u \equiv \nabla^2(T_e\Phi/e)/\rho_s^2$. In addition, length ≡ length × ρ_s. As a matter of fact, we report the following scale for turbulence in CSDX. Here, we use normalized density fluctuations $\tilde{n}/n_0$ to calculate $\bar{k}_r$

$B(G)$	800	900	1000	1200	1300
ρ_s (cm)	1.40	1.24	1.12	0.93	0.86
$L_n^{-1}(\mathrm{cm}^{-1})$	0.53	0.55	0.6	0.62	0.5
$\bar{k}_r(\mathrm{cm}^{-1})$	0.33	0.33	0.37	0.32	0.34
$1/[2.3\rho_s^{0.6}L_n^{0.3}]$	0.29	0.32	0.34	0.39	0.37

Thus

$$l_0 = \bar{k}_r^{-1} = 2.3\rho_s^{0.6}L_n^{0.3} \sim \rho_s$$

as L_n and ρ_s are of the same order before the transition occurs. Similarly, the Rhines' scale $l_{Rh} \sim \rho_s$, as it involves a radial derivative proportional in turn to ρ_s. We mention here that these results are clearly affected by the low values of $\rho^* = \rho_s/a$ in CSDX. Further studies at lower ρ^* are clearly needed. The potential enstrophy $\varepsilon = (n - \rho_s^2\nabla_\perp^2\Phi)^2/2 = (n - \rho_s^2k_\perp^2\Phi)^2/2 = (n - (\rho_s/l_{mix})^2\Phi)^2/2$ does not depend explicitly on B, as both n and $\rho_s k_\perp = \rho_s/l_{mix}$ are explicitly B-independent. With both the perpendicular ion diffusivity D_c and viscosity μ_c proportional to $1/B^2$, we obtain the following B-dependent equations:

$$\omega_{ci}\partial_t n = \partial_x\left[\frac{\varepsilon^{3/2}l_0^2\partial_x n}{\varepsilon + l_0^2\left(\partial_x\left(n - u/\rho_s^2\right)\right)^2} + D_c\partial_x n\right] + S, \tag{10a}$$

$$\omega_{ci}\partial_t u = \partial_x\left[\frac{\varepsilon^{3/2}l_0^2\partial_x u}{\varepsilon + l_0^2\left(\partial_x\left(n - u/\rho_s^2\right)\right)^2} + \mu_c\partial_x u\right], \tag{10b}$$

$$\omega_{ci}\partial_t\varepsilon = \partial_x\left[\frac{\varepsilon^{3/2}l_0^2\partial_x\varepsilon}{\varepsilon + l_0^2\left(\partial_x\left(n - u/\rho_s^2\right)\right)^2}\right] + L^2\left[\frac{l_0^2\varepsilon^{3/2}\left(\partial_x\left(n - u/\rho_s^2\right)\right)^2}{\varepsilon + l_0^2\left(\partial_x\left(n - u/\rho_s^2\right)\right)^2} - 2\varepsilon^{3/2} + \sqrt{\varepsilon}\right]. \tag{10c}$$

2. Numerical techniques and model calculation

A finite difference method with a fixed space step size and adaptive time step sizes is used. The boundary conditions used here are: $n|_{x=1} = u|_{x=1} = \partial_x n|_{x=0} = \partial_x\varepsilon|_{x=0} = \partial_x\varepsilon|_{x=1} = \partial_x u|_{x=0} = 0$. Note that Neumann boundary conditions are imposed on ε at both ends of the domain to prevent energy inflow/outflow from or to the system. As a trial case, we use the following initial profiles: $n(x,0) = (1-x)\exp[-ax^2 + b]$, $u(x,0) = cx^2 + dx^3$ and $\varepsilon(x,0) = (n(x,0)$

$-u(x,0))^2/2$ with $a=-5$, $b=0.125$, $c=1$, and $d=-1$. The initial density profile corresponds to a fitting of CSDX experimental data at $B=800\,G$. Initial vorticity and enstrophy profiles are arbitrary. Collisional Prandtl number $Pr=\mu_c/D_c=650\gg 1$ and a normalized mode scale length $l_0=1/5$ are used. We write the ion density source $S(x)$ as a shifted Gaussian: $S(x)=S(1-x)\exp\left[-(x-x_0)^2/e\right]$, where $x_0=0.7$, $e=0.05$, and S is the source amplitude. This form of density source is justified by the fact that radially injected neutrals become ionized at a normalized radial position $x_0=0.7$, as revealed by the decreasing (increasing) radial profile measurements of neutrals (ions). These radial variations are insensitive to any change in the axial location of the probe along the magnetic field axis. As for the amplitude S, the ionization rate corresponding to the conditions of CSDX experiments implies a normalized value of $S=10^4$.

In addition to calculating the plasma profiles at different B values to relate to CSDX experiments, we perform a scan of the external ion density fueling source and calculate the profiles at different S values. The latter corresponds to a change in the heating power of CSDX. Unless stated otherwise, we will use the following code colors throughout the paper: $B_{blue}<B_{red}<B_{green}<B_{black}$. Figure 2 shows radial variations of the density profiles for an increasing magnetic field B and two ion source amplitudes $S=10$ and $S=10^4$. The latter corresponds to a CSDX experiment. Similar to experimental results, a steepening trend in the mean density profiles is observed in both cases, as B increases. This steepening is clearly noticeable in the range $0.2<x<0.5$ for the $S=10^4$ case.

A closer look at the $S=10^4$ density profiles shows that a density peak initially observed at the injection location $x_0=0.7$ appears to shift inward as B increases. Moreover, the peaking of density profiles close to the center as B increases suggests the existence of an inward flux. This begs

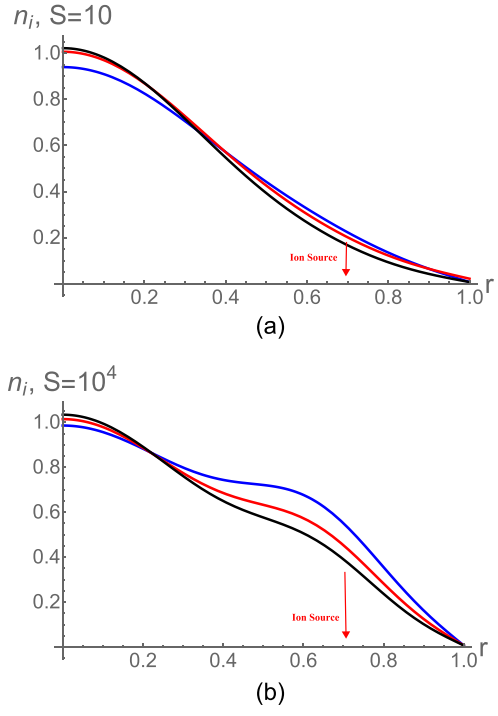

FIG. 2. Density profiles for $S=10$ and $S=10^4$ for increasing B.

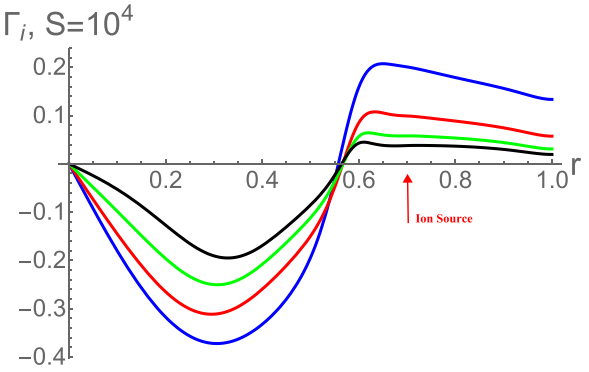

FIG. 3. Fluxes for $S=10^4$ for increasing B.

then the following questions: what is this apparent inward particle flux due to? Does it develop as a response to an increasing B? Is it inherent to the dynamics? To answer these questions, we investigate variations of the radial particle flux as a function of an increasing B. Figure 3 shows reduction in the particle transport, i.e., a reduction in Γ_n, as B is increased, for an ion density source $S=10^4$. This occurs as a result of the decrease of the diffusion coefficient $D_n=l_{mix}^2\varepsilon^{1/2}$ with B (see Fig. 4). The calculated profiles in Fig. 3 also imply an inward Γ_n for $0<x<0.5$. Experimentally, the apparent inward particle flux was reported to increase in response to an increasing B. This feature however does not appear in the model. We emphasize here though that for a helicon plasma source, the RF input power into the source varies with B. This leads to a variation in the amplitude of the ion density source S. Typically, one would manually adjust this power in order to keep the ion density source constant. However, this step was not implemented in CSDX experiments. One might therefore indirectly relate a change in B to a corresponding change in the particle flux profiles via variations of the density source S. This option is not considered here, as S magnitude is kept constant throughout the simulations.

Examining Fig. 5(a), the particle flux corresponding to $S=10$ is always outward (positive). This suggests that the experimental apparent inward flux is rather the result of the increasing amplitude of the off-axis density source S, and not a direct consequence of an increasing magnetic field B. We test this conjecture by holding B constant and increasing S. We find that Γ_n starts to go negative in the device core for increasing S values, at constant B, as shown in Fig. 5(b). Here, $S_{blue}=10$, $S_{red}=30$, $S_{green}=50$, and $S_{black}=10^4$. Moreover, at sufficiently long times, the calculated particle flux saturates, and Γ_n profiles are positive and show no indication of inward flux (Fig. 6). We conclude then that the

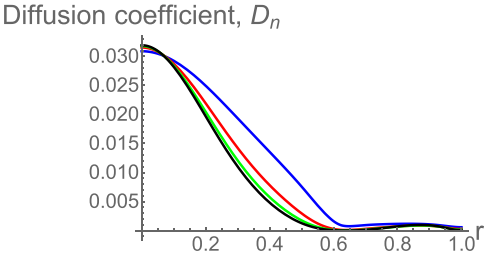

FIG. 4. Diffusion coefficient for increasing B.

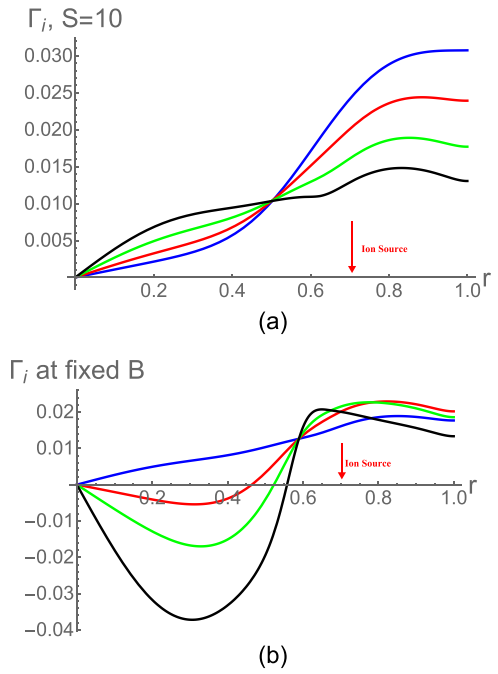

FIG. 5. Particle flux at $S = 10$ for increasing B and particle flux at constant B and increasing S : $S_{blue} < S_{red} < S_{green} < S_{black}$.

experimentally reported apparent inward flux appears to be a consequence of a change in the source amplitude and its position. Thus, we recover the apparent inward flux *semi-qualitatively*, using a diffusive model for $\Gamma_n = -\partial_x n$ (no particle pinch V_{pinch}, i.e., no off-diagonal term in Γ_n). It is essential to note here that experiments corresponding to different heating powers have been performed in CSDX. Data

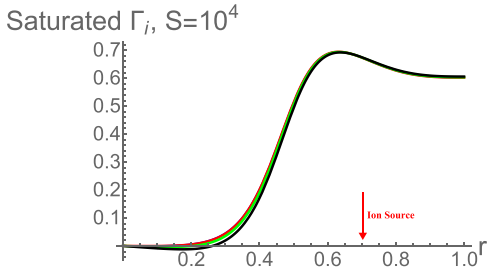

FIG. 6. Purely outward particle flux at sufficiently long time.

collected from these experiments show a dependence of both the direction and the amplitude of the particle flux Γ_n on the input heating power. Further investigation of these data is of crucial importance to fully understand the nature of this apparent inward flux.

In order to determine if the model captures the DW-ZF interactions in CSDX, we examine variations of the shear flow and of the Reynolds work with B. Figure 7(a) shows the existence of an azimuthal velocity shear layer in the radial direction that gradually becomes stronger as B increases. This shear does not depend on the ion source intensity S. The Reynolds force $-\partial_x \langle \tilde{V}_x \tilde{V}_y \rangle$ applied by turbulence on the flow increases in absolute value with B [Fig. 7(b)]. Variation rates of the Reynolds work P_{Re} done by the turbulence on the flow, i.e., the net shear flow production rates, also increase in absolute value [Fig. 7(c)]. This indicates an enhanced turbulence suppression as B increases. We note that the same values are obtained either by direct numerical computations or by multiplication of the Reynolds force by the absolute values of the azimuthal velocity. In summary,

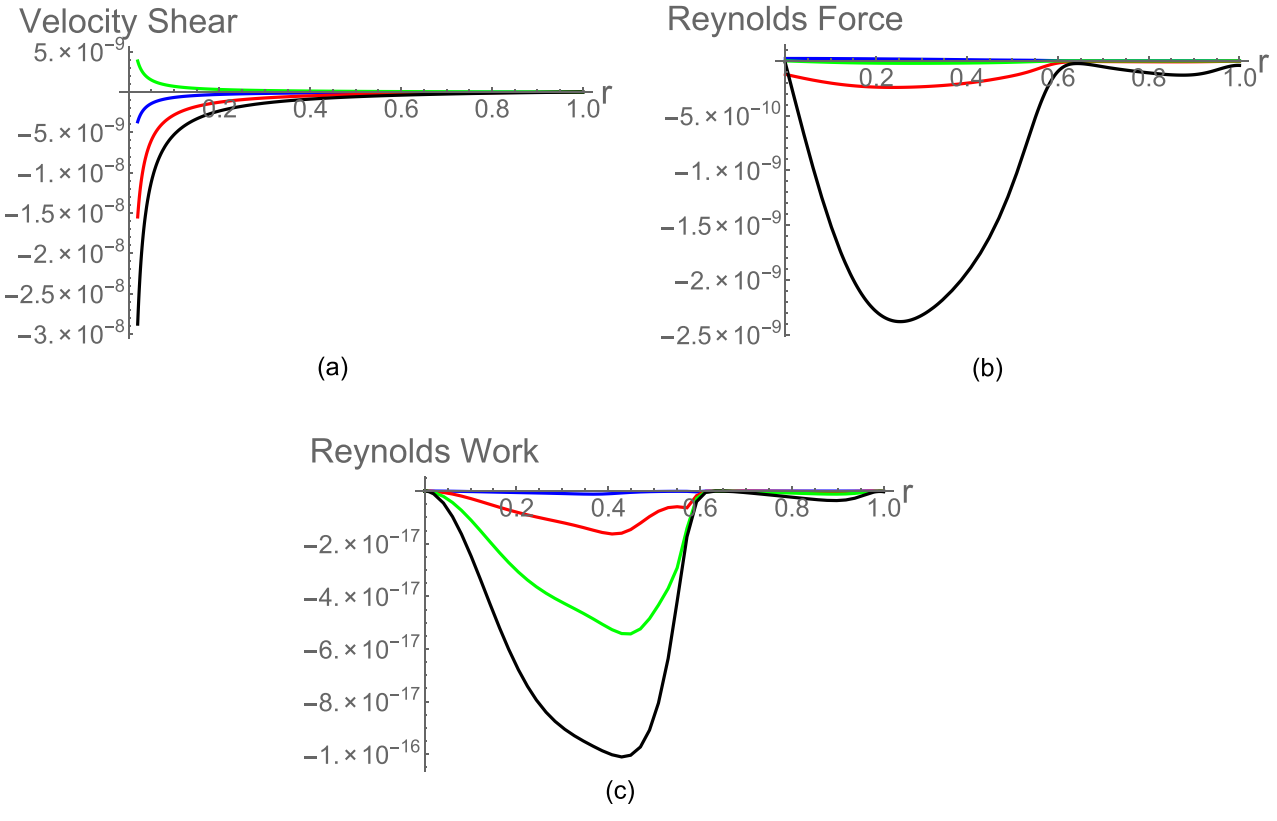

FIG. 7. Velocity shear, Reynolds Force, and Reynolds work for increasing B at $S = 10^4$.

steepening of the density profiles, amplification of the azimuthal velocity shear, and negative Reynolds work values are all indications of turbulence reduction that intensifies, as B increases. As B rises, Reynolds force increases and reinforces the plasma flow. At the same time, the corresponding cross-field ion turbulence scale length ρ_s decreases, allowing for more energy transfer from the microscopic scales to the mesoscopic ones. These observations were reported experimentally in Refs. 41–43, when applying cross-bispectral analysis to density and potential fluctuations data retrieved from CSDX.

B. Vorticity Flux with Residual Stress: $\Pi=\Pi_{res}-\chi\partial_x u$

Next we study the system dynamics when a residual $\Pi_{res} = (\chi - D_n)\partial_x n$ is included in the vorticity flux expression. The 3-fields equations become

$$\partial_t n = \partial_x[D_n\partial_x n] + D_c\partial_x^2 n + S(x), \tag{11a}$$

$$\partial_t u = \partial_x[(D_n - \chi)\partial_x n] + \partial_x[\chi\partial_x u] + \mu_c\partial_x^2 u, \tag{11b}$$

$$\partial_t \varepsilon = \partial_x[D_\varepsilon\partial_x\varepsilon] + \Pi_{res}(\partial_x n - \partial_x u) - (\chi\partial_x u - D_n\partial_x n) \times (\partial_x n - \partial_x u) - \varepsilon^{3/2} + \sqrt{\varepsilon}(u_0^2 - \varepsilon). \tag{11c}$$

Here, we use the following diffusion coefficients: $D_n = l_{mix}^2\varepsilon/\alpha$, $D_\varepsilon = l_{mix}^2\varepsilon^{1/2}$ and $\chi = l_{mix}^2\varepsilon/\sqrt{\alpha^2 + c_u u^2}$. Using the same scaling factors as before in addition to: $\alpha \equiv u_0\alpha$ and $c_u \equiv c_u/L^2$, we obtain the following B-dependent equations:

$$\omega_{ci}\partial_t n = \partial_x\left[\frac{l_0^2\varepsilon^2\partial_x n}{\varepsilon + l_0^2\left(\partial_x\left(n - u/\rho_s^2\right)\right)^2}\frac{1}{\alpha} + D_c\partial_x n\right] + S, \tag{12a}$$

$$\omega_{ci}\partial_t u = \rho_s^2\partial_x\left[\frac{l_0^2\varepsilon^2}{\varepsilon + l_0^2\left(\partial_x\left(n - u/\rho_s^2\right)\right)^2} \times \left[\left(\frac{1}{\alpha} - \frac{1}{\sqrt{\alpha^2 + c_u\left(u/\rho_s^2\right)^2}}\right)\partial_x n + \left(\frac{1}{\sqrt{\alpha^2 + c_u\left(u/\rho_s^2\right)^2}} + \mu_c\right)\partial_x u\right]\right], \tag{12b}$$

$$\omega_{ci}\partial_t\varepsilon = \partial_x\left[\frac{l_0^2\varepsilon^{3/2}\partial_x\varepsilon}{\varepsilon + l_0^2\left(\partial_x\left(n - u/\rho_s^2\right)\right)^2}\right] + L^2\left[\frac{l_0^2\varepsilon^2\rho_s}{\varepsilon + l_0^2\left(\partial_x\left(n - u/\rho_s^2\right)\right)^2)} \times \left(-\frac{1}{\alpha} + \frac{1}{\sqrt{\alpha^2 + c_u\left(u/\rho_s^2\right)^2}}\right) \times \left(\partial_n - \frac{\partial_x u}{\rho_s^2}\right) - \frac{l_0^2\varepsilon^2}{\varepsilon + l_0^2\left(\partial_x\left(n - u/\rho_s^2\right)\right)^2} \times \left(-\frac{\partial_x}{\alpha} + \frac{1}{\sqrt{\alpha^2 + c_u\left(u/\rho_s^2\right)^2}}\frac{\partial_x u}{\rho_s^2}\right) \times \left(\partial_x n - \frac{\partial_x u}{\rho_s^2}\right) - 2\varepsilon^{3/2} + \sqrt{\varepsilon}\right]. \tag{12c}$$

We show here numerical results that correspond to both Dirichlet and Neumann vorticity boundary conditions at $x = 1$. Starting with a Dirichlet condition $u|_{x=1} = 0$, for an arbitrary case $\alpha = 3$ and $c_u = 6$ trial case, numerical results are similar to those obtained when no residual stress is included in the expression of Π. The steepening of the density profiles, the sheared azimuthal velocity layer, and the negative Reynolds work values in the three left figures of Fig. 8 are all consistent with a global transition that occurs in the plasma as B increases. Variation of the shearing coefficient c_u, which reflects a change in the strength of the flow shear, does not seem to affect qualitatively the numerical results (right three figures of Fig. 8); the results are simply insensitive to a change in c_u. Therefore we conclude that, while Π^{res} is needed to account for intrinsic rotation in tokamaks and axial flow generation in linear devices,[39] a state of enhanced confinement can be recovered using a simple diffusive form of the vorticity flux, without the need to include a residual stress in the expression for Π.

The scenario of a plasma column surrounded by a layer of fixed neutrals next to the walls corresponds to a Neumann vorticity boundary condition: $\frac{\partial u}{\partial x}|_{x=1} = 0$. Viscous effects are negligible in this case. We mention here though that the usual experimental case corresponds to a Dirichlet boundary condition. Steepening of the density profiles and negative Reynolds work values are recovered as a sign of turbulence suppression, as B increases. The velocity shear, although present and prominent at the density steepening location, is B independent (top three figures of Fig. 9). Higher magnetic field values are required for this B-dependence to appear. The Reynolds work becomes then positive (bottom three figures of Fig. 9). The latter suggests turbulence production by the flow at high B values, i.e., an instability that might be triggered by the vorticity gradient at high B instead of being suppressed by the velocity shear.

A change in the mode scale length from $l_0 = \rho_s/5$ to $l_0 = 10^{-3}\rho_s$ leads to the same previously mentioned trends of turbulence suppression as indicated by density profile steepening, negative Reynolds work values, and a B dependent sheared azimuthal velocity (see Fig. 10).

More interesting is the relevant case of a higher Prandtl number $Pr = \mu_c/D_c = 65000$. In this case, momentum diffusivity dominates the behavior of the plasma characterized by a low diffusion coefficient D_c. Figure 11 shows time evolution of the plasma profiles at consecutive times t_1 and t_2. The plasma density builds up at the injection location and the inward flux develops as a result of density localized concentration, regardless of the magnitude of B. Evidence of a turbulence suppression such as negative Reynolds work rates and sheared azimuthal velocity is also recovered.

IV. VALIDATION METRICS FOR MODEL COMPARISON WITH EXPERIMENT

Going beyond the simple qualitative comparisons between numerical and experimental profiles, we propose here a set of quantitative metrics which aim to test whether the adopted model equations are indeed capable of explaining the experimental observations. Quoting Oberkampf and

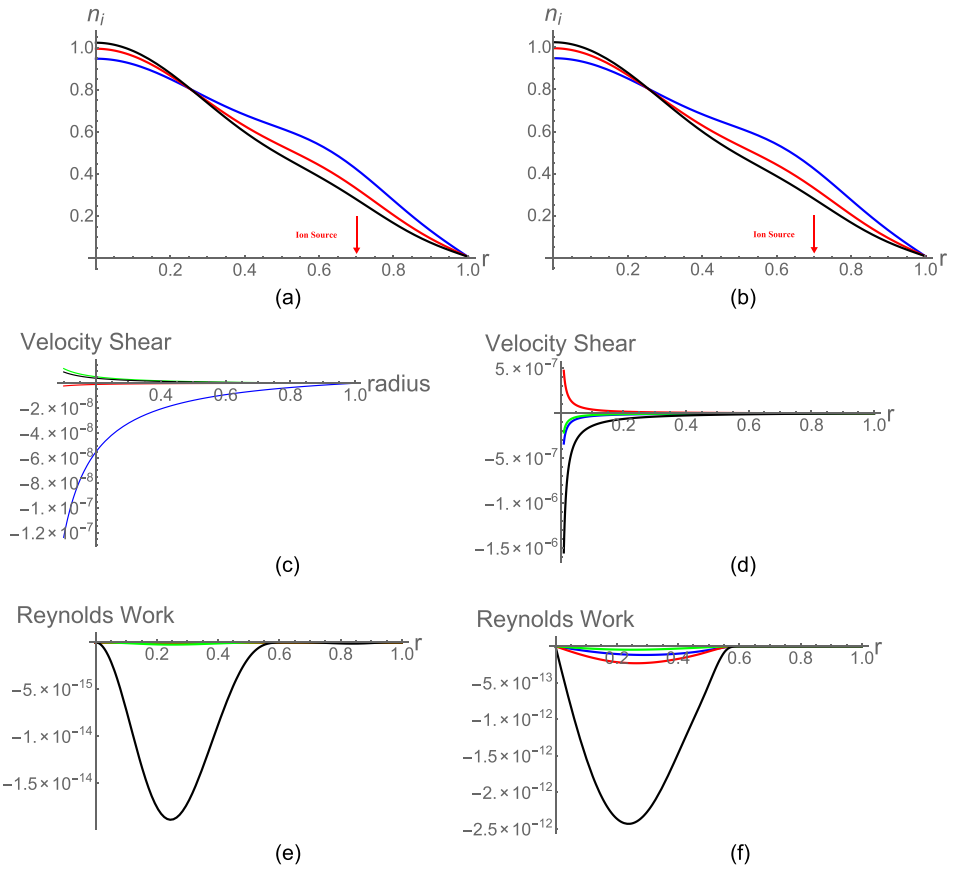

FIG. 8. Profiles with Π_{res} and Dirichlet boundary conditions for $c_u = 6$ and $c_u = 600$.

Trucano (2002)," an important issue concerns how comparisons of computational results and experimental data could be quantified" (p.216).[44] A set of validation metrics is therefore needed to check the consistency of the model with the experimental data.[45] We start first by checking the relative variation of the inverse density gradient scale length $1/L_n = |\nabla \ln n|$ and recover a value close the experimental one obtained from profiles of Fig. 2 in Ref. 26,

$$\frac{\Delta(1/L_n)}{L_{n_i}} = \frac{1/L_{n_f} - 1/L_{n_i}}{1/L_{n_i}} = \begin{cases} 0.70 & \text{numerically} \\ 0.55 & \text{experimemtally.} \end{cases}$$

Here, $1/L_{n_i}$ ($1/L_{n_f}$) is the inverse gradient scale length of the initial (final) density profile, i.e., before (after) the plasma transition occurs. Similarly, we calculate the corresponding relative variation of the inverse gradient scale length of the velocity profiles and find

$$\frac{\Delta(1/L_v)}{L_{v_i}} = \frac{1/L_{v_f} - 1/L_{v_i}}{1/L_{v_i}} = \begin{cases} 0.73 & \text{numerically} \\ 0.57 & \text{experimentally.} \end{cases}$$

While the previous validation metrics constitute *local* assessment quantities, we also propose two *global* validation metrics. Figure 12 is a plot of the radially integrated Reynolds work, $P_{Re-tot} = \int_0^1 P_{Re} dr$ which denotes the total work done by turbulence on the flow over the plasma cross section as a function of the density gradient. $1/L_n$ and P_{Re-tot} are proportional to each other; as B increases, density profiles steepen, the ion gradient scale length L_n shrinks and the total Reynolds work rate increases, indicating a transfer of energy from fluctuations to flow.

Further validation of turbulence suppression is obtained by examining the particle loss rate $1/\tau_{turb-loss}$, due to turbulent radial transport. This rate is expected to drop as B increases. Integration of the particle flux along r gives values of the loss rates: $1/\tau_{turb-loss} \propto \int_0^r r\Gamma_n dr$. Data reported in Table I show a declining trend as B increases. This suggests a change in the global particle balance, i.e., a change in the nature of the turbulence in the system.

V. WHAT IS THE CRITERION FOR TURBULENCE SUPPRESSION?

A conceptual question in modeling drift wave-zonal flow turbulence is the prediction of when transport barriers are triggered. A variety of proposals are on record. Most are equivalent to a comparison of linear growth rate to $E \times B$ shearing rate (i.e., $|\gamma_L|$ vs. $|\gamma_{E\times B}|$). The relevance of this type of criterion to fully developed turbulence is, at best, unclear. A somewhat non-trivial criterion,[28] is $R_T > 1$ where

$$R_T = \frac{\langle \tilde{v}_x \tilde{v}_y \rangle' v_{E\times B}}{|\gamma_{eff}| \langle \tilde{v}_\perp^2 \rangle} \tag{13}$$

is the local ratio of the Reynolds power density, to the effective increase in turbulent kinetic energy. Here, $|\gamma_{eff}|(\nabla n, \nabla T, V_{ZF})$ is the turbulence effective growth rate. The idea here is that when $R_T > R_{Tcrit}$ (usually $R_{T_{crit}} \sim 1$), the energy transfer to the shear flow exceeds the effective increase in

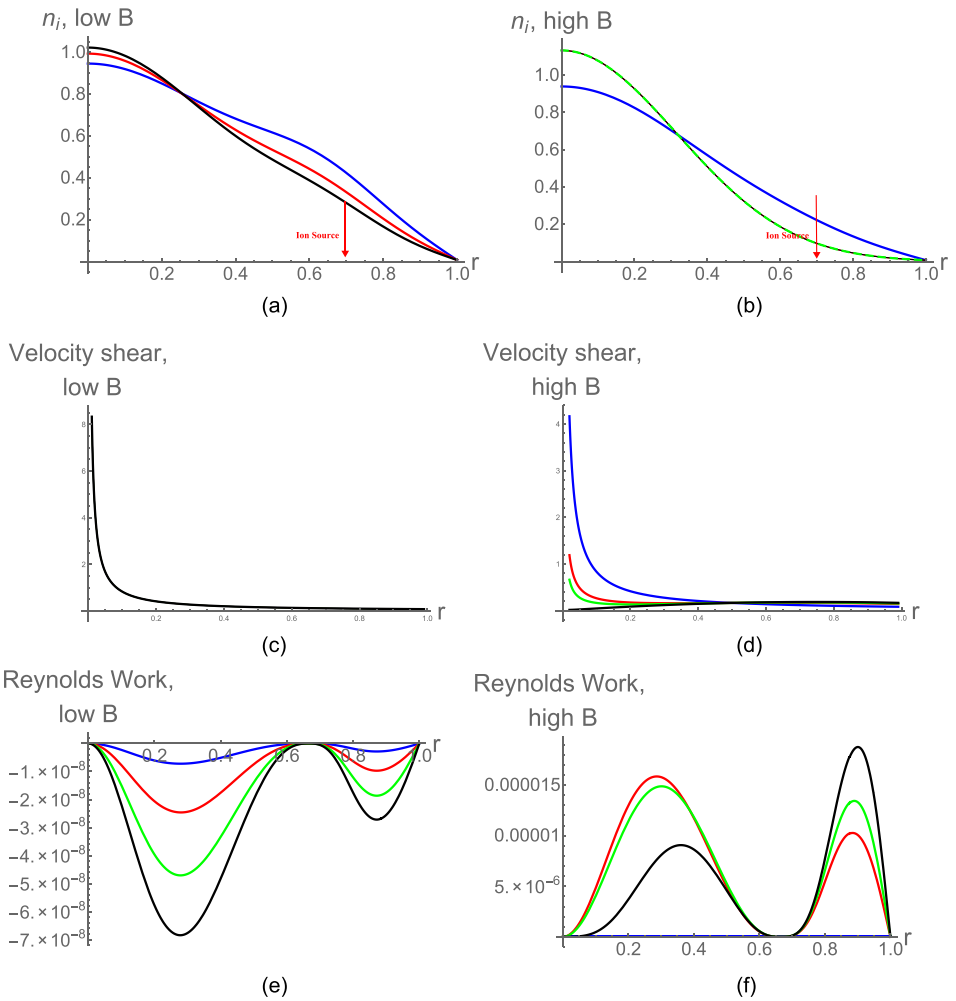

FIG. 9. Profiles with Π_{res} and Neumann boundary conditions for increasing B.

turbulent kinetic energy, suggesting a collapse of the $k_\theta \neq 0$ portion of the turbulence spectrum, i.e., the part which causes transport. For the model under study here, the instantaneous potential enstrophy growth rate is $|\gamma_{eff}| = (1/\varepsilon).(\partial\varepsilon/\partial t)$ and $\langle \tilde{v}_\perp^2 \rangle = \varepsilon l_{mix}^2 = l_0^2\varepsilon^2/(\varepsilon + (l_0\nabla(n-u))^2)$. Figure 13 shows variations of R_T with B for this system. Here, R_T values are calculated at the density steepening location and at the turbulent energy saturation time. The proportionality between B and R_T is recovered as anticipated, since an increase in B triggers the formation of transport barriers.

While the $R_T > R_{Tcrit}$ criterion is attractive for its extreme simplicity, it suffers from the facts that: i) $|\gamma_{eff}|$ is ill-defined, and difficult to calculate, ii) contributions from energy other than the kinetic are ignored. Thus, we propose

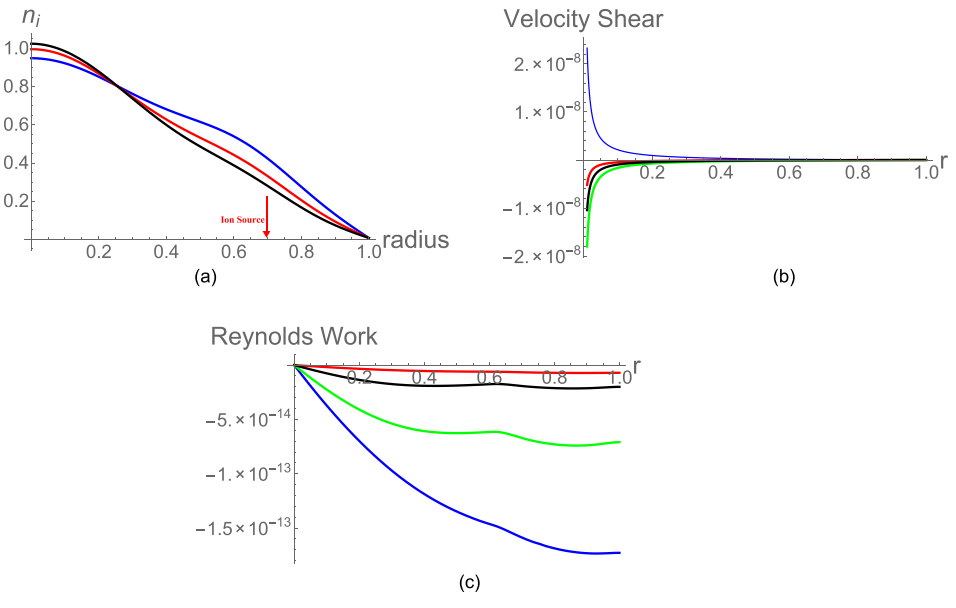

FIG. 10. Profiles for $l_0 = 10^{-3}\rho_s$ and increasing B.

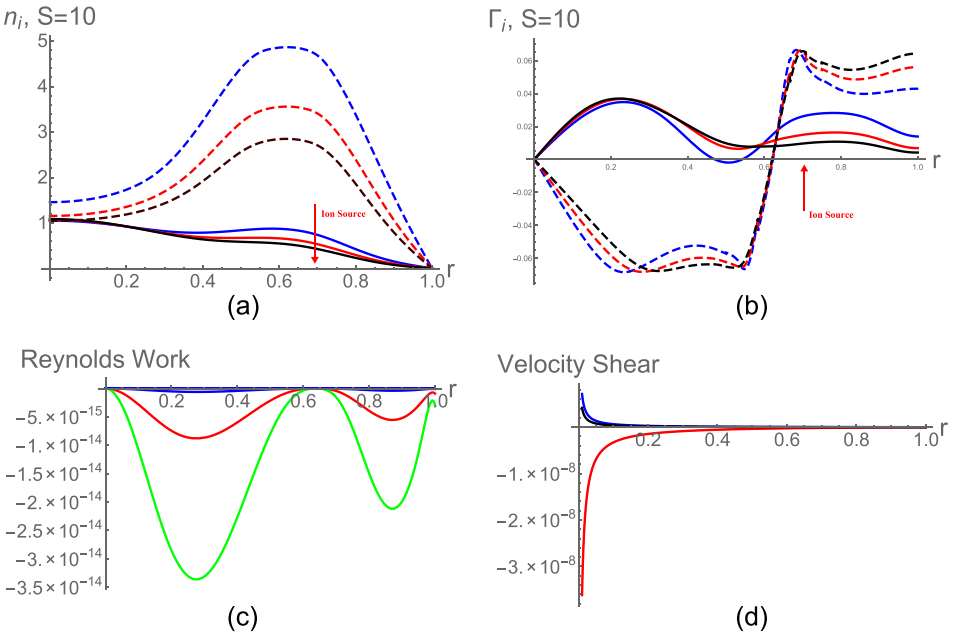

FIG. 11. Profiles for $Pr = 65000$ and increasing B. Solid and dashed plots correspond to data at t_1 and t_2, respectively.

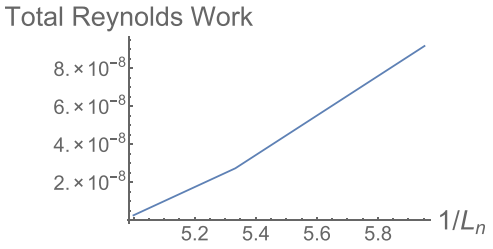

FIG. 12. P_{Re-tot} as function of $1/L_n$ for increasing B.

here an alternate criterion, $R_{DT} \geq R_{DT_{crit}}$, where the global parameter $R_{DT} = \tau_{relax}/\tau_{transfer}$. Here, $1/\tau_{relax} = -\int dx \Gamma_n \nabla n/n_0$, where $\Gamma_n = \langle \tilde{v}_x \tilde{n}/n_0 \rangle$ is the normalized particle flux, $1/\tau_{relax}$ is the rate of relaxation of the free energy source, which is ∇n in this model. Of course, ∇n relaxes by exciting drift wave turbulence, so $1/\tau_{relax}$ is effectively the turbulent enstrophy production rate and would have a connection to the energy input rate, $|\gamma_{eff}|$, used in the R_T criterion. Logically then, that should be compared to the rate of transfer of enstrophy to the mean flow vorticity profile. This may be thought of a turbulent enstrophy destruction rate, and is closely related to the Reynolds work which appears in R_T. We have then: $1/\tau_{transfer} = -\int dx \langle \tilde{v}_x \tilde{u} \rangle \nabla u$ where $u = \rho_s^2 \nabla_\perp^2 (e\Phi/T_e)$. Integrating by parts gives: $1/\tau_{transfer} = \int dx \partial_x \langle \tilde{v}_x \tilde{u} \rangle u$ so,

$$R_{DT} = \frac{\int \partial_x \langle \tilde{v}_x \tilde{u} \rangle u dx}{-\int \Gamma_n \nabla n/n_0 dx} \tag{14}$$

TABLE I. Particle loss rate $1/\tau$ for increasing B.

$1/\tau_{\text{loss}}$ ($\times 10^{-2}$)	$S = 10$	$S = 50$	$S = 10^4$
B_{blue}	1.4	3	1.1
B_{red}	1.2	2.6	0.5
B_{black}	0.9	1.8	0.2

R_{DT} is manifestly dimensionless and the integrals are calculated along the radius. Noting the Taylor identity and the fact that $u \sim \nabla_\perp(\nabla_\perp \Phi) \sim \nabla_\perp V_y$, the correspondence of the numerator of R_{DT} to that of R_T is evident. Finally, given that the potential vorticity is conserved on fluid particle trajectories, it is not difficult to see the correspondence between fluctuating entropy ($\sim -\int dv(\delta f)^2/\langle f \rangle$) and fluctuating enstrophy. Thus, R_{DT} may be thought of as the ratio of fluctuation entropy destruction via coupling to the mean flow, to fluctuating entropy production via relaxation of ∇n. Both numerator and denominator reflect flux-gradient interaction and both emerge naturally from the formulation of the model, i.e., from expanding the production term $P_{prod} = (\Gamma_n - \Pi).(\nabla n - \nabla u) = \underline{\Gamma_n \nabla n} + \underline{\Pi \nabla u} - \Pi \nabla n - \Gamma_n \nabla u$ in Eq. (2c). Neglecting the last two cross terms in P_{prod}, the numerator and denominator of R_{DT} simply represent the product of Π and ∇u, and Γ_n and ∇n, respectively. Thus, R_{DT} exceeding unity may be thought of as the simplification of the more general criterion that $\int P_{prod}$ passes through zero, i.e., $\int P_{prod} > 0 \rightarrow \int P_{prod} < 0$, as the indicator of turbulence collapses. Figure 14 shows variations of R_{DT} with B at the same time and location as for R_T. The close relation between R_{DT} and B can also be interpreted in terms of enstrophy exchange of fluctuations to flow, as B increases. However,

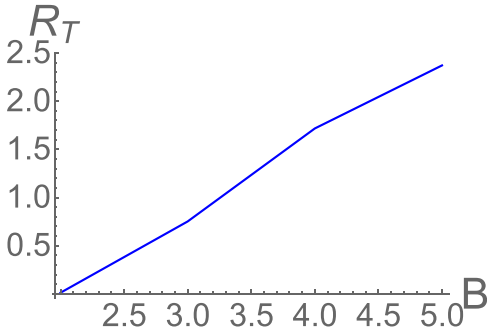

FIG. 13. R_T time variations at $x = 0.1$, 0.6, and 0.8 (Blue, Green, and Brown) for $S = 40$.

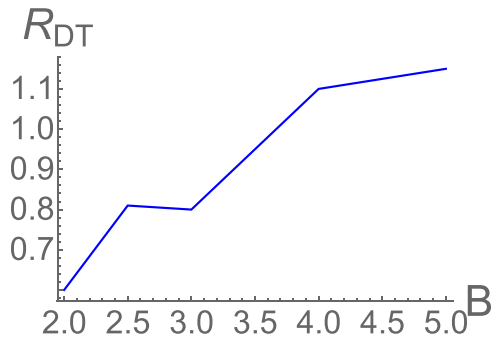

FIG. 14. R_{DT} variations for $S = 10$ and increasing B.

the $R_{DT} > R_{DT_{crit}}$ criterion has a broader and more solid theoretical foundation than $R_T > R_{T_{crit}}$, and easily may be generalized (to more complex models) by expanding the consideration of potential enstrophy balance. When either R_{DT} or R_T exceeds unity, the turbulence levels will drop and a barrier is likely to be formed. We do not have a proof of either though - particularly given the ambiguity in just exactly what a barrier is.

VI. DISCUSSION AND CONCLUSIONS

Features of a CSDX improved confinement are reproduced here using a 1D time-dependent reduced model. The model recovers the profile evolution in CSDX with an increasing B, and includes both a slow and a fast time scale: the former corresponding to the time evolution of the mean fields, and the later corresponding to turbulence production and fast dissipation. Potential enstrophy is conserved up to dissipation and initial forcing. Inhomogeneous PV mixing is a central feature here, and occurs on a mixing length that is inversely proportional to the PV gradient. The use of a mixing length that shrinks as ∇n and ∇u steepen closes the positive feedback loop on PV. The model novelty relies in the fact that it reduces the profile evolution to only two fluxes: a vorticity and a density flux.

Numerical solutions agree with the experimental findings, and show: a steepening of the density profile, a reinforced $E \times B$ sheared layer, an increased Reynolds work, and a reduction in the turbulence and particle transport, as B increases. Numerical solutions also show that the steepening of ∇n is recovered without the use of an off-diagonal term nV_{pinch} in the expression of the particle flux Γ_n. The experimentally apparent inward flux is simply of diffusive nature at high B. Moreover, the model predicts qualitatively similar results, with or without the inclusion a residual stress Π_{res} in the vorticity flux expression Π. We conclude then the following: both density and vorticity fluxes have purely diffusive forms: $\Gamma_n = -\partial_x n$ and $\Pi = -\partial_x u$, where u is the vorticity. The inward pinch V_{pinch} and residual stress Π_{res} necessary to drive axial flows in linear devices are not required to recover the experimental results. As a matter of fact, the validation metrics presented above show a consistent level of agreement between computation and experiment, using purely diffusive expressions for Γ_n and Π.

The only experimental feature not recovered is the apparent inward particle flux. The apparent inward flux, experimentally believed to be related to increasing B, is a direct consequence of the amplitude and location of the ion source. Additional investigation of the influence the fueling intensity might have on the particle flux is crucial to determine the nature of this inward flux.

The energy parameter R_{DT}, defined in Eq. (14), emerges as a better global turbulence collapse indicator to be used in the future. It rests on a broader and more solid theoretical foundation than R_T, and can be obtained both in computations and experiments. In addition, R_{DT} includes the basic physics behind R_T, but transcends it. Finally, modeling of the parallel flow dynamics is planned for future work. This will be pursued by adding an equation for $v_{\|}$ to the model.

ACKNOWLEDGMENTS

This research was supported by the U.S. Department of Energy Grant under Award Nos. DE-FG02–04ER54738 and DE-SC0008378. We thank T. Stoltzfus-Dueck, A. Diallo, R. Hong, and S. Thakur for useful discussions. R. Hajjar also thanks P. Vaezi for useful discussions.

[1]W. Horton, Rev. Mod. Phys. **71**, 735 (1999).
[2]X. Garbet, Plasma Phys. Controlled Fusion **43**, A251 (2001).
[3]M. A. Malkov, P. H. Diamond, K. Miki, J. E. Rice, and G. R. Tynan, Phys. Plasmas **22**, 032506 (2015).
[4]L. Schmitz, L. Zeng, T. L. Rhodes, J. C. Hillesheim, E. J. Doyle, R. J. Groebner, W. A. Peebles, K. H. Burrell, and G. Wang, Phys. Rev. Lett. **108**, 155002 (2012).
[5]G. R. Tynan, M. Xu, P. Diamond, J. Boedo, I. Cziegler, N. Fedorczak, P. Manz, K. Miki, S. Thakur, L. Schmitz, L. Zeng, E. Doyle, G. M. McKee, Z. Yan, G. S. Xu, B. N. Wan, H. Q. Wang, H. Y. Guo, J. Dong, K. Zhao, J. Cheng, W. Y. Hong, and L. W. Yan, Nucl. Fusion **53**, 073053 (2013).
[6]P. H. Diamond, S. I. Itoh, K. Itoh, and T. S. Hahm, Plasma Phys. Controlled Fusion **47**, R35 (2005).
[7]M. J. Burin, G. R. Tynan, G. Y. Antar, N. A. Crocker, and C. Holland, Phys. Plasmas **12**, 052320 (2005).
[8]G. Y. Antar, J. H. Yu, and G. Tynan, Phys. Plasmas **14**, 022301 (2007).
[9]H. Arakawa, K. Kamataki, S. Inagaki, T. Maruta, Y. Nagashima, T. Yamada, S. Shinohara, K. Terasaka, S. Sugita, M. Yagi, N. Kasuya, A. Fujisawa, S.-I. Itoh, and K. Itoh, Plasma Phys. Controlled Fusion **51**, 085001 (2009).
[10]T. Klinger, A. Latten, A. Piel, G. Bonhomme, and T. Pierre, Plasma Phys. Controlled Fusion **39**, B145 (1997).
[11]P. H. Diamond, O. D. Gurcan, T. S. Hahm, K. Miki, Y. Kosuga, and X. Garbet, Plasma Phys. Controlled Fusion **50**, 124018 (2008).
[12]B. A. Carreras, V. E. Lynch, L. Garcia, and P. H. Diamond, Phys. Fluids B **5**, 1491 (1993).
[13]F. L. Hinton, Phys. Fluids B **3**, 696 (1991).
[14]H. Biglari, P. H. Diamond, and P. W. Terry, Phys. Fluids B: Plasma Phys. **2**, 1 (1990).
[15]T. S. Hahm and K. H. Burrell, Phys. Plasmas **2**, 1648 (1995).
[16]T. Estrada, T. Happel, C. Hidalgo, E. Ascasíbar, and E. Blanco, EPL (Europhys. Lett.) **92**, 35001 (2010).
[17]S. J. Zweben, R. J. Maqueda, R. Hager, K. Hallatschek, S. M. Kaye, T. Munsat, F. M. Poli, A. L. Roquemore, Y. Sechrest, and D. P. Stotler, Phys. Plasmas **17**, 102502 (2010).
[18]G. S. Xu, B. N. Wan, H. Q. Wang, H. Y. Guo, H. L. Zhao, A. D. Liu, V. Naulin, P. H. Diamond, G. R. Tynan, M. Xu, R. Chen, M. Jiang, P. Liu, N. Yan, W. Zhang, L. Wang, S. C. Liu, and S. Y. Ding, Phys. Rev. Lett. **107**, 125001 (2011).
[19]S. H. Muller, J. A. Boedo, K. H. Burrell, J. S. deGrassie, R. A. Moyer, D. L. Rudakov, W. M. Solomon, and G. R. Tynan, Phys. Plasmas **18**, 072504 (2011).
[20]U. Stroth, T. Geist, J. P. T. Koponen, H.-J. Hartfuß, P. Zeiler, and ECRH and W7-AS Team, Phys. Rev. Lett. **82**, 928 (1999).
[21]T. Kobayashi, S. Inagaki, Y. Kosuga, M. Sasaki, Y. Nagashima, T. Yamada, H. Arakawa, N. Kasuya, A. Fujisawa, S.-I. Itoh, and K. Itoh, Phys. Plasmas **23**, 102311 (2016).

[22]S. Zhou, W. W. Heidbrink, H. Boehmer, R. McWilliams, T. Carter, S. Vincena, S. K. P. Tripathi, P. Popovich, B. Friedman, and F. Jenko, Phys. Plasmas **17**, 092103 (2010).
[23]G. R. Tynan, C. Holland, J. H. Yu, A. James, D. Nishijima, M. Shimada, and N. Taheri, Plasma Phys. Controlled Fusion **48**, S51 (2006).
[24]S. C. Thakur, C. Brandt, L. Cui, J. J. Gosselin, A. D. Light, and G. R. Tynan, Plasma Sources Sci. Technol. **23**, 044006 (2014).
[25]L. Cui, G. R. Tynan, P. H. Diamond, S. C. Thakur, and C. Brandt, Phys. Plasmas **22**, 050704 (2015).
[26]L. Cui, A. Ashourvan, S. C. Thakur, R. Hong, P. H. Diamond, and G. R. Tynan, Phys. Plasmas **23**, 055704 (2016).
[27]A. Ashourvan and P. H. Diamond, Phys. Rev. E **94**, 051202 (2016).
[28]K. Miki, P. H. Diamond, O. D. Gurcan, G. R. Tynan, T. Estrada, L. Schmitz, and G. S. Xu, Phys. Plasmas **19**, 092306 (2012).
[29]A. Hasegawa and M. Wakatani, Phys. Rev. Lett. **50**, 682 (1983).
[30]A. Hasegawa and M. Wakatani, Phys. Rev. Lett. **59**, 1581 (1987).
[31]S. C. Thakur, J. J. Gosselin, J. McKee, E. E. Scime, S. H. Sears, and G. R. Tynan, Phys. Plasmas **23**, 082112 (2016).
[32]S. Inagaki, T. Kobayashi, S. I. Itoh, T. Mitsuzono, H. Arakawa, T. Yamada, Y. Miwa, N. Kasuya, M. Sasaki, M. Lesur, A. Fujisawa, and K. Itoh, Sci. Rep. **6**, 22819 (2016).
[33]J. C. Li and P. H. Diamond, Phys. Plasmas **24**, 032117 (2017).
[34]A. Ashourvan, P. H. Diamond, and O. D. Gurcan, Phys. Plasmas **23**, 022309 (2016).
[35]P. B. Rhines, J. Fluid Mech. **69**, 417 (1975).
[36]W. D. Smyth and J. N. Moum, Phys. Fluids **12**, 1327 (2000).
[37]P. Diamond, C. McDevitt, D. Gürcan, T. Hahm, W. X. Wang, E. Yoon, I. Holod, Z. Lin, V. Naulin, and R. Singh, Nucl. Fusion **49**, 045002 (2009).
[38]O. D. Gurcan, P. H. Diamond, and T. S. Hahm, Phys. Rev. Lett. **100**, 135001 (2008).
[39]J. C. Li, P. H. Diamond, X. Q. Xu, and G. R. Tynan, Phys. Plasmas **23**, 052311 (2016).
[40]N. J. Balmforth, S. G. Llewellyn Smith, and W. R. Young, J. Fluid Mech. **355**, 329 (1998).
[41]P. Manz, M. Xu, S. C. Thakur, and G. R. Tynan, Plasma Phys. Controlled Fusion **53**, 095001 (2011).
[42]M. Xu, G. R. Tynan, C. Holland, Z. Yan, S. H. Muller, and J. H. Yu, Phys. Plasmas **16**, 042312 (2009).
[43]Z. Yan, G. R. Tynan, C. Holland, M. Xu, S. H. Muller, and J. H. Yu, Phys. Plasmas **17**, 012302 (2010).
[44]W. L. Oberkampf and T. G. Trucano, Prog. Aerospace Sci. **38**, 209 (2002).
[45]C. Holland, Phys. Plasmas **23**, 060901 (2016).